NUMERICAL DESIGN OF RESONATOR COILS FOR HIGH FIELD MAGNETIC RESONANCE IMAGING

A Thesis

Presented in Partial Fulfillment of the Requirements for the Degree Bachelor of Science in the Graduate School of The Ohio State University

By

Jacob James Adams

******

The Ohio State University

2005

Honors Thesis Examination Committee:

Dr. Robert Lee, Advisor

Dr. Robert Garbacz

ABSTRACT

In the past, design of transmit/receive coils for magnetic resonance imaging was performed using simple lumped circuit models; however, as developments in technology have allowed for increasingly high magnetic fields, the frequency at which the imaging must be performed has increased to the hundreds of megahertz, causing technical difficulties to arise. This project seeks to overcome the problem of inhomogeneous magnetic excitation through a redesign of the resonator coil based in electromagnetic theory. Several designs were attempted, with the primary modifications being in the dielectric filling and length of the resonator.

Since the lumped circuit model is no longer valid at today's high fields, it must be replaced by a full-wave electromagnetic solution. Therefore, all simulations for this project were performed with a FDTD program previously developed at Ohio State for this purpose.

The simulations have shown that a significant increase in homogeneity can be achieved by loading the resonator with a high permittivity dielectric. This in turn lowers the resonant frequency, so the cavity length must be shortened to raise the frequency back to normal values. The best case design found here is with a 10 cm resonator filled with relative dielectric of 60. A better design can likely be found with a resonator of approximately 8 cm in length, but this was unable to be tested due to

technical difficulties and time constraints. The project also confirms that dielectric loading of a certain region will cause the field peak to shift towards the load. This could be useful for locating the field peak at a certain point in the head in order to obtain an MRI image in just that area.

ACKNOWLEDGMENTS

Thank you to all those who have helped in the completion of this project. The biggest thanks go to my thesis advisor Prof. Rob Lee who has spent a great deal of time helping me understand this project. I would also like to thank Anca Stefan who has been instrumental in helping me use and modify the FDTD code. The professors at OSU who have motivated my interest in research and electromagnetics deserve a thank you as well. Finally, I would like to thank my parents and girlfriend who have always been supportive and helped me take care of those everyday things that often go unnoticed, but without which this project would not have been possible.

VITA

September 8, 1982.....Born – Columbus, Ohio

June 2002 – June 2004.....Student Research Assistant, The ElectroScience Lab, The Ohio State University

June 2004 - August 2004.....Intern, RF Apertures, Northrop Grumman – Baltimore, MD

September 2004 – present.....Student Research Assistant, The Ohio State University

TABLE OF CONTENTS

LIST OF FIGURES

CHAPTER 1

INTRODUCTION

Nuclear magnetic resonance imaging (MRI) is a widely known medical procedure used to observe the internal structure of the human body in both clinical practice and biomedical research. First introduced in the 1970's [1], MRI holds key advantages over other imaging techniques in that it is non-invasive and poses no risk to the patient. Furthermore, MRI has multiple imaging modalities, high contrast between different tissues, and is easily used for three dimensional imaging [2]. These numerous advantages place MRI at the forefront of medical imaging research, and the continued refinement of imaging capabilities is critical to advances in clinical medicine and biomedical research.

The first chapter of this paper will outline the fundamentals of magnetic resonance imaging with a focus on electromagnetic behavior. Then in the second and third chapters, the transverse electromagnetic (TEM) resonator simulated in this project will be described, along with the numerical method used to perform these simulations. Finally, the simulation results will be presented in the fourth chapter, followed by a brief conclusion and discussion of future work in this area.

1.1 Purpose and Goals

An MRI image is obtained by applying a strong static magnetic field to a body and then exciting the nuclear spins of the body with a radio frequency (RF) pulse. The excited protons then emit a second RF signal ("echo") which can be received and processed into an image. In the past 30 years, magnet capability has increased dramatically, with strengths today ranging from a few thousand Gauss to 9.4 Tesla (T) (1 Tesla = 10,000 Gauss) for whole body imaging [3]. Working at higher field strengths has significant imaging benefits; however, due to technical challenges at the higher field strengths, clinical MRI is still typically done at 1.5 T.

At high fields, faster scan times are observed, and there are large improvements in image quality due to increased signal-to-noise ratio (SNR) [4]. Another useful application of high field imaging is functional MRI (fMRI), a procedure used to detect the levels of oxygen in the blood. Through this procedure, a functional map of the brain can be developed by measuring the local oxygen saturation while providing different stimuli. This method relies on the blood oxygenation level dependent (BOLD) contrast which has been shown to be greatly enhanced at high fields [5].

In order to take advantage of these benefits, the technical barriers encountered at high fields must be overcome. One of the most challenging problems when moving to higher field systems is RF field inhomogeneity caused by the increased resonant frequency of the target nuclei which, at high fields, is a few hundred megahertz [6]. Possible solutions to this problem are improved RF coil/resonator designs or alternate imaging modalities that do not rely upon homogeneous RF field

distribution within the coil. The ultimate goal of this project is to develop RF resonators that will improve the quality of high-field MRI images that can be obtained, primarily for the human head. The project will largely be a continuation of work begun in the doctoral dissertation of Tamer S. Ibrahim [7]. In order to improve RF magnetic field distribution and by consequence, image quality, modifications to the standard transverse electromagnetic (TEM) resonator coil will be explored.

1.2 The Physical Phenomenon of Magnetic Resonance

Magnetic resonance imaging is rooted in the physical phenomenon of nuclear magnetic resonance (NMR) which was first studied in the 1940s [8]. This phenomenon involves the application of a static magnetic field to a proton or other particle with non-zero spin. Please note that this treatment will look at NMR in the classical sense only and is simplified to illustrate the concepts most clearly. This approach is sufficient for our purposes, but there are many more detailed treatments available in textbooks [2, 9].

Consider a free proton with an intrinsic spin which gives the particle a magnetic dipole moment, μ along its axis of rotation. When a static magnetic field is applied, the moment aligns itself with the field and given no other excitation, will remain aligned. However, an interesting effect is observed when an RF excitation is applied with the magnetic component of the wave perpendicular to the static field. The magnetic moment of the proton is tipped away from the static field axis and begins to precess around the static field. This precession can be sustained if the excitation is at a certain resonant frequency. Figure 1.1 illustrates this process.

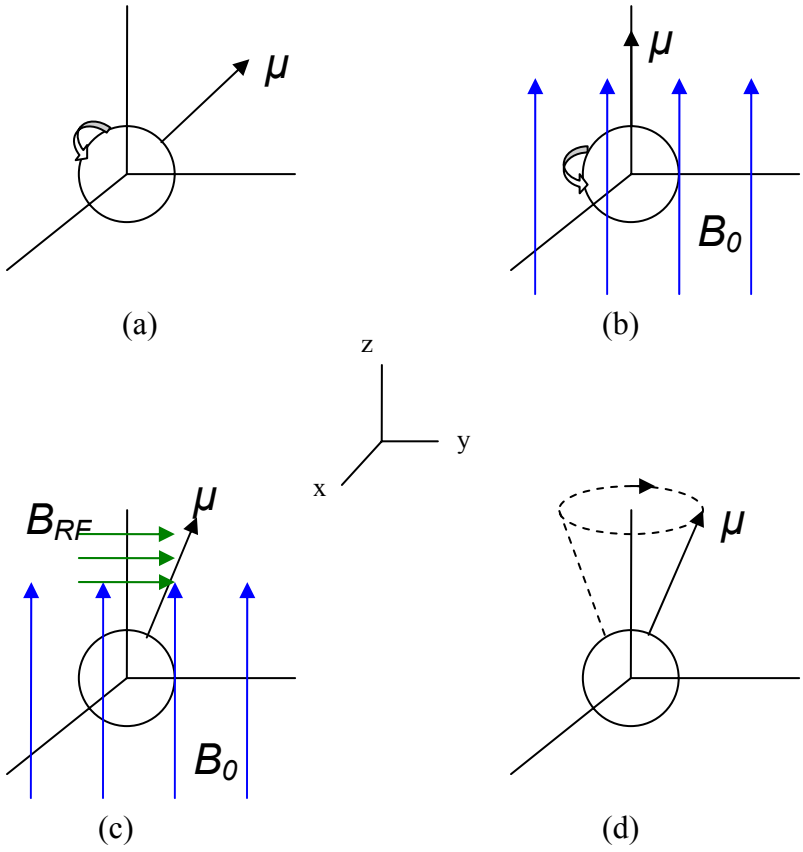

Figure 1.1: Simplified illustration of nuclear magnetic precession. Randomly oriented spin (a) is rotated to align with an applied static B field (b). An RF magnetic field is then excites the proton spin perpendicular to the static field and tips it away from the static field axis (c). If the RF field is at the Larmour frequency, precession about the static field begins (d).

Another way to visualize the motion is to think of the proton as a spinning top with the angular momentum vector of the top equivalent to the magnetic moment of the proton and the static magnetic field perpendicular to the table. Once the top is spun, it will precess about its tip which touches the table until its energy is lost to friction. This is somewhat like the NMR motion.

The frequency at which the proton's resonance occurs is known as the Larmour frequency and is given by [9]

$$\omega_{res} = \gamma |B_0| \tag{1.1}$$

where γ is a material-dependent constant known as the gyromagnetic ratio. For hydrogen this value is 2.675 x 10^8 rad/s/T. Elements that can be imaged using MRI include ^{1}H, ^{2}H, ^{7}Li, ^{13}C, ^{19}F, ^{23}Na, ^{31}P, and ^{127}I [2]. These elements can be imaged because they have a non-zero magnetic moment.

Beyond the basic principles of NMR, there are some topics which are important to MRI specifically. A normal MRI sequence consists of exciting magnetized atoms with a brief RF pulse and then receiving an RF pulse "echo" as the atoms return to their unexcited state. In order to understand the echo signal that is received, it is important to discuss polarization, flip angle, relaxation times, static field gradients, and imaging sequences.

1.3 Polarization of the RF Excitation and Flip Angle

Consider a rotating coordinate frame (F') that circles a proton at the Larmour frequency, ω_{res} in the clockwise sense. In the laboratory (rest) frame, a linearly polarized RF excitation pulse at the Larmour frequency is given by

$$B_1^{lin} = b_1 \cos(\omega_{res} t) \tag{1.2}$$

By coordinate transformation, this pulse appears in the rotating frame as [9]

$$B_1^{lin} = \frac{1}{2} b_1 [\hat{x}'(1 + \cos(2\omega_{res} t)) + \hat{y}' \sin(2\omega_{res} t)] \tag{1.3}$$

where x' and y' are the unit vectors in F'. If we then take the time average value of the RF field in the rotating frame, we find

$$\left\langle B_1^{lin} \right\rangle = \frac{1}{2} b_1 \hat{x}' \tag{1.4}$$

which shows that only half of the total power of the pulse can be used in the rotating frame. Since the precessing proton's dipole moment exists wholly in F', only half of the input pulse power can be used to tip the pulse. This is remedied by exciting with a left-hand circularly polarized (LHCP) pulse,

$$B_1^{LHCP} = b_1[\hat{x}\cos(\omega_{res}t) - \hat{y}\sin(\omega_{res}t)] \tag{1.5}$$

which gives a constant value of b_1 in the x' direction and allows the full input power to be used in tipping the dipole moment away from the z axis. It should also be noted that a right hand circularly polarized (RHCP) wave will have zero magnitude in the F' frame, and will be unable to tip the proton's spin [7]. For simplicity, we define the left hand circular wave as B^+ and the right hand wave as B^-.

Observing the rotating frame F' given in Figure 1.2, it can be seen that the precessing proton spin will appear at an angle θ from the z' axis. This is known as the flip angle and is given by [2]

$$\theta = \gamma \int_0^{\tau} B_1^+(t)\ dt \tag{1.6}$$

where τ is the pulse duration.

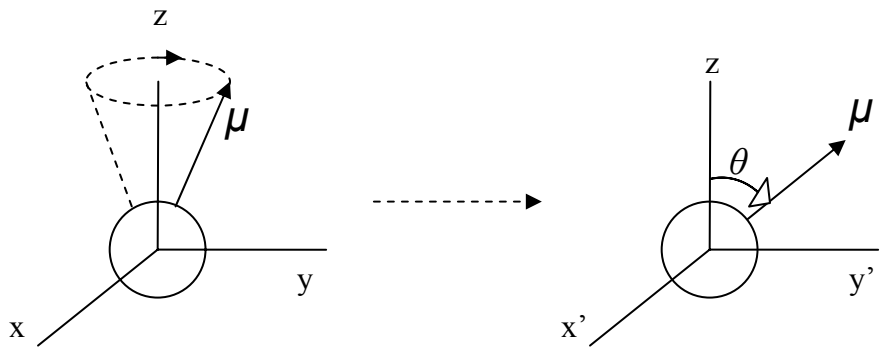

Figure 1.2: The transformation from the laboratory frame to the primed frame rotating clockwise at the Larmour frequency. The flip angle θ is shown.

1.4 Relaxation Times

After the spins are tipped away from the z axis, the net magnetization they form will begin to decay. There are two types of decay that affect the magnetization; they are the T1 and T2 relaxation times. The relaxation times are useful because they differ from tissue to tissue. Thus, they can be used to differentiate between them.

The T1 time is known as the spin-lattice relaxation time or longitudinal relaxation time. The T1 relaxation effect begins after the RF pulse has ended. It represents the return of the spins to their "ground" state along the z axis. This means the magnetization along the x'y' plane decreases and also experiences regrowth along z. The decay in x'y' is an exponential proportional to [9]

$$M_{x'y'} \propto e^{-t/T_1} \tag{1.7}$$

However, in many applications the T1 time can be discounted in the x'y' plane because it is often much larger than the time a scan takes, making the decay insignificant.

The T2 time is called the spin-spin relaxation time or transverse relaxation time. This decay occurs because of small static field inhomogeneities caused by interactions with other particles within the sample [9]. Because Eq. 1.1 says that the Larmour frequency is proportional to the static B-field, each position will have slightly different resonant frequencies. This leads to "dephasing" of their individual magnetizations in the x'y' plane and a net exponential decrease in magnetization similar to Eq. 1.7. Dephasing is the "fanning out" of the individual magnetization vectors and is illustrated in Figure 1.3 with a 90˚ flip angle as an example.

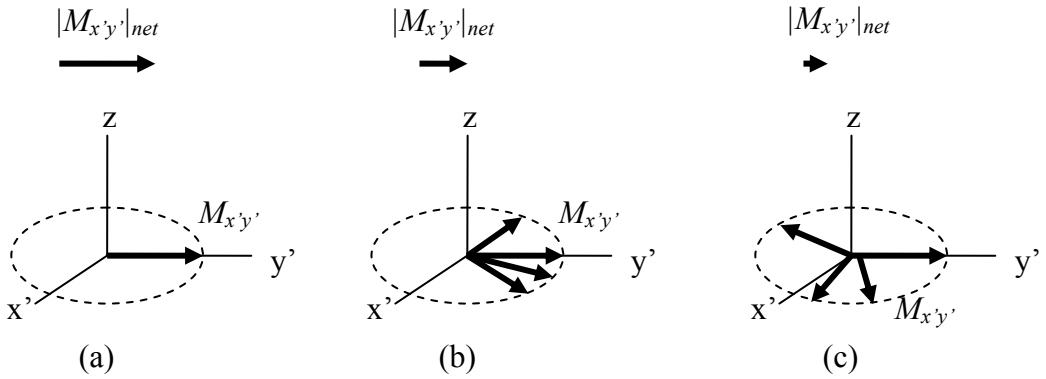

Figure 1.3: Dephasing due to transverse relaxation. At first all magnetizations are aligned along y' (a). After some time, they begin to dephase, with those precessing faster than the theoretical Larmour frequency moving ahead in phase and those processing slower moving further behind (b, c).

1.5 Field Gradients and Imaging Sequences

In order to image in multiple dimensions at the same time, there must be a way to differentiate between signals coming from different locations. A simple way of doing this is to use a slight gradient in the static B field in one direction. Then, in that direction, the Larmour frequency will vary with the static field strength as per Eq. 1.1. In exciting such a sample, the ideal RF pulse is a square wave in frequency over the band of Larmour frequencies created by the field gradient. When the echo signal is received, the different spatial locations can be differentiated by separating the received frequencies. This is called frequency encoding. Imaging in two and three dimensions can be accomplished by phase encoding in addition to frequency encoding. This method is covered in any textbook on MRI techniques.

The two primary imaging sequences are spin echo and gradient echo imaging. The goal of each is to produce an "echo" in the transverse (x'y' plane) magnetization which can be received and processed. In spin echo imaging, the echo is achieved by exciting the resonance with a 90˚ RF pulse and then letting the magnetizations

dephase in the transverse plane as in Figure 1.3. Next, a 180˚ pulse is applied which inverts the pulses on the x'y' plane and allows them to rephase. When they are completely rephased, an echo is emitted as the magnetizations line up for a moment.

Gradient echo imaging is similar to spin echo, but it uses a static field gradient in the z direction to dephase the spins after an RF pulse. Again, the spins are dephasing because they are precessing at different frequencies, in this case caused by the field gradient. The gradient is then reversed and the spins rephase to form an echo.

Based on which features of the sample need to be seen, these two echo techniques can produce image contrast based on proton density, T1, or T2. These are known as proton density weighted, T1 weighted, or T2 weighted images, respectively.

CHAPTER 2

THE TRANSVERSE ELECTROMAGNETIC RESONATOR

The physical device used to transmit and receive the RF pulses in MRI is often called the "RF coil". In some cases, two separate RF coils are used to transmit and receive, but in most applications, a single RF coil both transmits the excitation pulse and receives the echo from the sample. There have been many types of coils introduced, with each successive generation improving upon the last. Prior to the introduction of the transverse electromagnetic (TEM) resonator in 1994 [10], the birdcage resonator was the most widely used [11]. The TEM resonator has several advantages over the birdcage coil in improved excitation field homogeneity, high quality (Q) factor, and it is easily tuned [7].

2.1 Geometry of the TEM Resonator

The TEM resonator is a multi-transmission line structure as shown in Figure 2.1. In Figure 2.2, the geometry and features of the resonator are detailed. The resonator consists of a cylindrical cavity bounded on all sides by conducting walls except two circular apertures at either end of the cylinder which are open to fit the head. The other salient feature of the resonator is the collection of struts that run the length of the cylinder. Although Figure 2.2 shows just four struts for illustrative

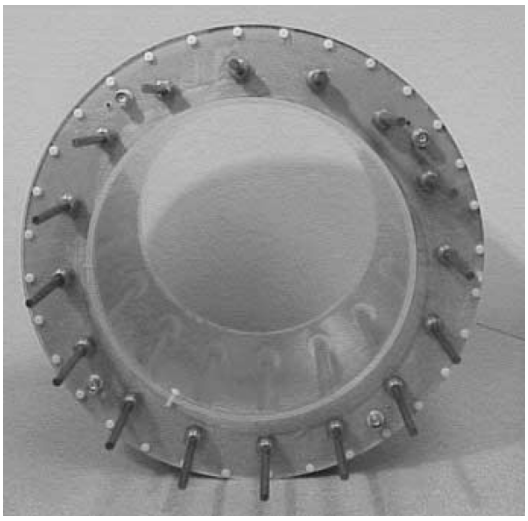

Figure 2.1: A photograph of a 16 strut TEM resonator.

purposes, there are typically more—8, 16, or 24 are more common. These struts are usually arranged along a circle concentric with the cylinder and consist of an inner and outer conductor separated by a dielectric sleeve. In conjunction with the conductive cylinder, this creates an eccentric coaxial transmission line with the struts as the inner conductors and the cavity walls as the outer conductor.

Each individual strut also acts as a coaxial line with the inner strut being the center conductor and the outer strut as the outer conductor. The inner strut has a gap in the center, and they can be pulled in and out of the resonator in order to tune it to the proper resonant frequency. It should be noted that the inner struts make electrical contact with the top and bottom end plates while the outer struts do not. Instead, the outer struts are electrically isolated by a small gap between the strut and the end plate. The resonator is driven by a source across this gap between the outer strut and end plate. Multi-port excitation is possible with the resonator, so it can be driven from as many struts as desired

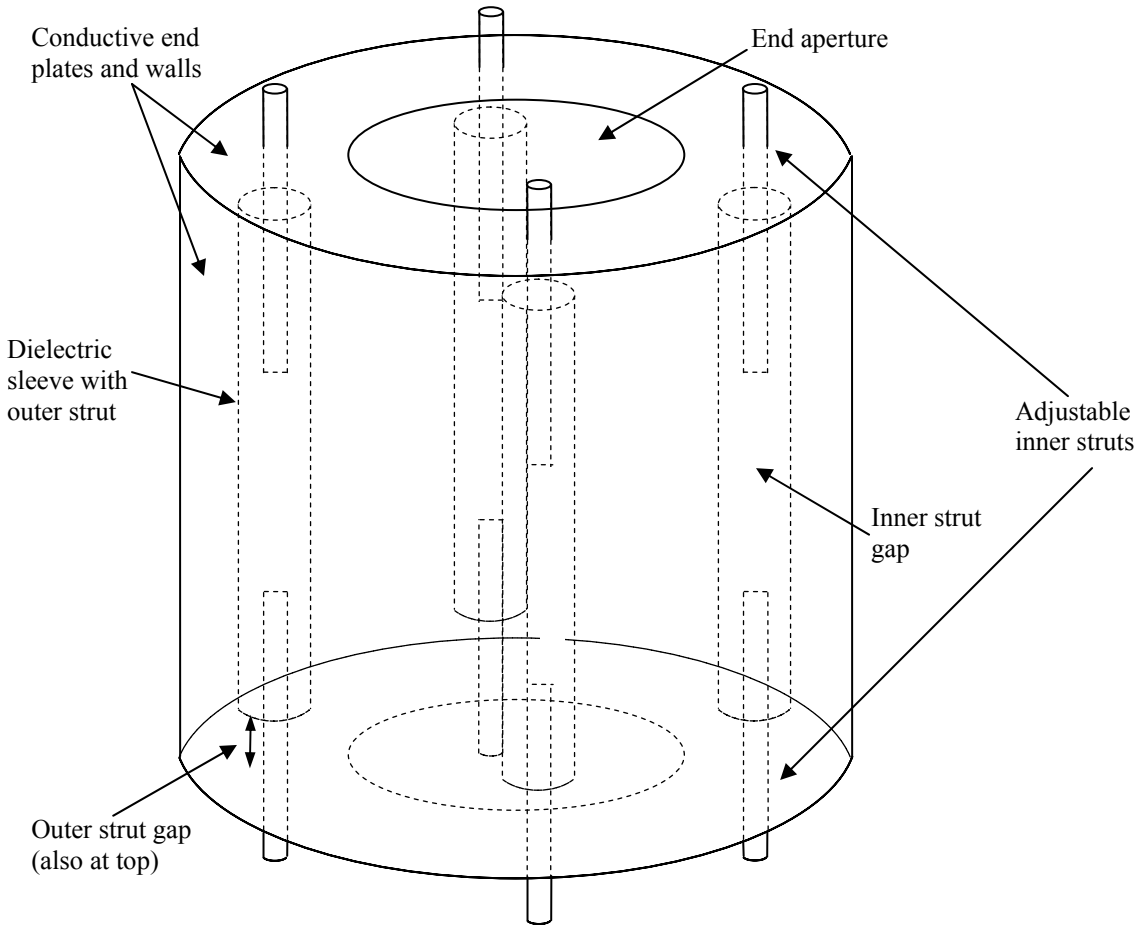

Figure 2.2: A schematic of the TEM resonator shows the prominent features of the device.

2.2 Theory of Operation of the Resonator

In the past, coils were modeled using lumped electrical elements in order to ensure operation at the Larmour frequency. This is appropriate with a low frequency excitation pulse (64 MHz at 1.5 T) where the size of the resonator and sample are a small fraction of a wavelength. However, at higher fields the resonant frequency increases to the point where the wavelengths are no longer much larger than the geometry of the resonator. For example, at 8 T the resonant frequency is nearly 343 MHz with a wavelength of less than 1 m. At this point, the lumped element model is

not valid and must be replaced with an electromagnetic solution that considers wave effects. A solution of the resonator has been completed using multiconductor transmission line theory, and it explains its operation [12].

The basic function of the resonator is to propagate a TEM wave in the axial direction (along the length of the cylinder). It first launches a wave into the strut coaxial line by applying a voltage across the small gap between the outer conductor and end plate. Since the end plate is in contact with the inner conductor, this same voltage appears across the gap from inner to outer conductor. This voltage moves down the strut until it reaches the open circuit termination where there is a gap between the two ends of the inner strut. Upon reflecting at this termination, the wave moves back up the line to the gap where it was launched. At this point it is launched into the large eccentric coax formed by the cylindrical cavity and struts where it propagates down as a TEM mode before reaching the other end plate and returning to the strut coaxial line [12].

Multiple modes can exist in the resonator because of the multi-transmission line structure. However, considering only TEM modes is a reasonable approximation for the empty resonator (i.e. no head inside) since hybrid modes will have cutoff frequencies higher than the frequency of operation. It has also been shown that an accurate model of the TEM modes can be developed without the use of hybrid modes for the empty resonator [12]. In this analysis by Baertlein *et al.*, it is found that an N-strut symmetric resonator will produce N/2+1 TEM modes. As an example, the theoretical frequency response of a 16 strut resonator is shown in Figure 2.3 [12]. The nine TEM modes appear clearly and agree with experimental results.

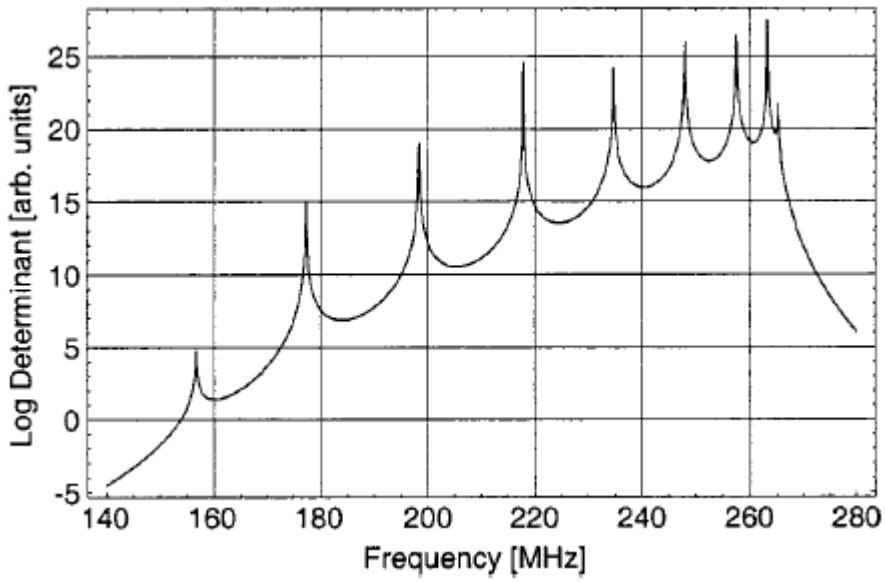

Figure 2.3: Typical frequency response of 16-strut resonator showing nine TEM modes. The second mode (175 MHz in this case) is the mode of interest for most MRI applications.

Now the modes must be examined to determine which is the most useful for head imaging. Magnetic field distributions of the first 6 modes are shown in Figure 2.4 [7]. These distributions have been calculated by a numerical code, but have also been verified with experimental results. Rather than directly representing the B^+ or B^- fields (left or right circularly polarized), the magnitude of fields for the plot are calculated as

$$|B| = |B_1^-| \sin(\gamma |B_1^+|) \qquad (2.1)$$

This normalized quantity is more useful for imaging purposes because it is proportional to the real signal received for an impulse excitation. It represents the actual MRI process because the B^+ signal initially excites the protons while the B^- signal is released in the echo. Thus both are important to obtaining a good image.

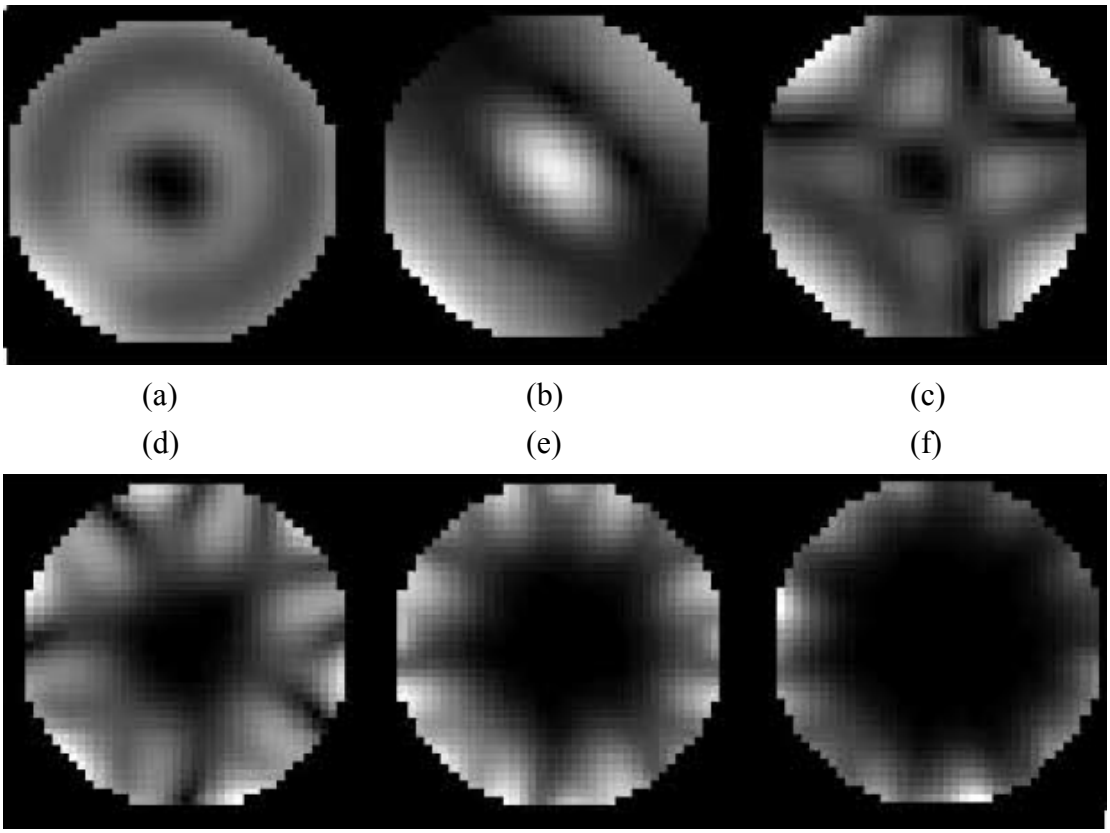

Figure 2.4: The normalized field distribution in the cavity for the first six modes of a 16-strut TEM resonator loaded with a saline phantom. Mode 0 (a) shows a clear null in the center while Mode 1 (b) shows the characteristic peak in the center with a null on the outer edge of the cavity. The higher order modes 2-5 (c-f) show various patterns, each with a null in the center.

From the field distributions in the cavity loaded with a saline bolus (Figure 2.4) [7], it is observed that of the six lowest-order modes, only Mode 1 (Figure 2.4b) has a field peak at the center. The three higher order modes that are not shown also have nulls in the center. In evaluating these distributions, we can conclude that Mode 1 is the most useful for typical imaging applications which measure nearer to the center of the head than the outer part. Because of this, Mode 1 will primarily be studied in the design portion of this work; however, it should be noted that Mode 0 is useful for fMRI brain function mapping. The portion of the brain which controls thought and sensory input is the cerebral cortex and is located around the outer parts of the skull where Mode 0 has its peak.

2.3 Field Inhomogeneity and Proposed Solution

As demonstrated in Figure 2.4, the main problem encountered when using the TEM resonator at high fields is the significant RF field inhomogeneities found across the sample. Ideally, the normalized field would be constant over the entire region of interest. With inhomogeneities as large as those for the high field TEM resonator, imaging can only be done over a small region. These inhomogeneities worsen when the resonator is loaded with a human head. The material in the human head is innately inhomogeneous and lossy; thus, by loading the formerly empty cavity, pure TEM modes can no longer be supported. Instead only hybrid modes exist in the cavity which tend to be inhomogeneous and are less effective than the TEM modes. For high field imaging, we expect that the left and right circular polarized components will have different distributions. This leads to even worse distributions for the normalized fields since both components contribute to the final image.

The proposed solution for this is to fill the empty parts of the cavity with a high permittivity dielectric material similar to the human head. This allows a more gradual transition from the TEM mode to the hybrid mode by lessening the material discontinuity. The resulting modes are expected to be closer to the TEM modes resulting in less inhomogeneity. The effect of this would a spreading of the central peak of Mode 1 to fill more of the cavity. This proposition is validated by earlier experimental results showing that more homogeneity was achieved by loading a different type of TEM resonator with titanium dioxide at 4 T [13]. The titanium dioxide can be processed to give a permittivity near that of the human brain.

There are some challenges involved with this solution, however. The complete filling of the cavity with a dielectric is impossible because a human test subject would not undergo such test conditions. Secondly, by increasing the permittivity inside the eccentric coaxial line, we shift the frequency response curve higher in frequency by the square root of the new permittivity. Since the human head has a permittivity of around 70, this will also be the target for filling the resonator. This means the frequency will be approximately 8 times higher than when the cavity is empty. In order to counter this, the resonator will be shortened by a factor of eight. This will scale the frequency response down so that Mode 1 is once again around 343 MHz for imaging at 8 T.

Additionally, another potential solution will be explored. Rather than trying to provide a homogeneous solution across the entire head, selective dielectric loading will be used to shift the central peak of Mode 1 to different locations. This will allow imaging in locations other than the center of the head.

CHAPTER 3

NUMERICAL METHODOLOGY

Because building a resonator and running trials with an 8 T machine is very expensive and time consuming, the studies in this paper are all done with computer simulation tools that have proven accurate in the past. As discussed earlier, the high Larmour frequency (343 MHz) at 8 T means that a full wave electromagnetic solution is necessary. The approach to solving this problem is discussed in the following chapter as well as the tools used to conduct simulations.

3.1 Approach to the Problem

Initially, it was known that the problem would be large and be likely to require a lot of computation time. Despite this, in order to have a user-friendly interface with which to test, the model of the resonator was created in Ansoft's High Frequency Structure Simulation (HFSS) commercial software which uses the finite element method (FEM). However, the program was unable to complete the simulation of the empty resonator because the adaptive meshing feature created a very fine mesh which required more memory than was available (1 GB).

Therefore, it was decided that the simulations must be completed using a custom application that had been used to numerically simulate TEM resonator designs in the past. This software was written at Ohio State by Anca Stefan in the Biomedical Engineering Program and uses the finite difference time domain (FDTD) method. The program is meant only as a research tool and is inherently less user-friendly than a commercial program like HFSS. Preparing, running, and analyzing a simulation takes several steps and requires running multiple applications during the process. However, the program has successfully modeled TEM resonator behavior at high frequencies in the past unlike HFSS which is unproven in this area.

After it was believed that the program was giving valid results with an unloaded cavity, some changes to the geometry and program were made, and analyses were conducted with a dielectric filling. As these results were considered, further changes to the geometry were carried out to explore the design space.

3.2 The Finite Difference Time Domain Method

The TEM resonator analysis code uses the finite difference time domain (FDTD) method to find the electric and magnetic field components over time. The FDTD method is one of the three primary numerical analysis methods in electromagnetics. The method of moments (MM) and finite element method (FEM) are also commonly used. Both the FEM and FDTD method solve for unknown electric and magnetic fields in the simulation area while the MM solves for unknown surface and volume currents on perfect electric conductors (PECs). Using the method of moments can significantly reduce the number of unknowns when only PEC and

perfect dielectrics are present, but this is not the case with the human head which is quite lossy. FEM analysis is conducted on a mesh which can be somewhat arbitrarily defined as long as it follows certain guidelines. This makes FEM a more flexible solution when solving complex geometries. However, FEM also requires solving a matrix equation which takes a great deal of computation. The FDTD method must use a grid of fixed size, but it is an iterative method that computes field values over a large number of time step and will solve a given number of unknowns faster than FEM [7]. Since this project will require a large number of simulations, the speed of the solution is important. Thus, because of this and because FDTD requires less memory than FEM, the FDTD method was chosen for this program.

The FDTD method was originally developed by Kane S. Yee in 1966 [14]. The method involves discretizing space and time with a geometry known as a Yee cell (Fig. 3.1) [7]. In the cell, the geometry of the problem is broken down into points on a cube, with H values appearing at the face centers and E values appearing at the edge centers. A function in this discretized space can be written as [7]

$$F^n(i,j,k) = F(i\Delta x, j\Delta y, k\Delta z, n\Delta t) \tag{3.1}$$

where Δx, Δy, Δz, and Δt are the steps in the x, y, and z direction and the time step.

To begin the formulation we have Maxwell's equations [7]

$$\vec{\nabla} \times \vec{E} = -\frac{\partial \vec{B}}{\partial t} - \sigma_m \vec{H} \tag{3.2}$$

$$\vec{\nabla} \times \vec{H} = \frac{\partial \vec{D}}{\partial t} - \sigma_e \vec{E} \tag{3.3}$$

$$\nabla \cdot \vec{D} = \rho_e \tag{3.4}$$

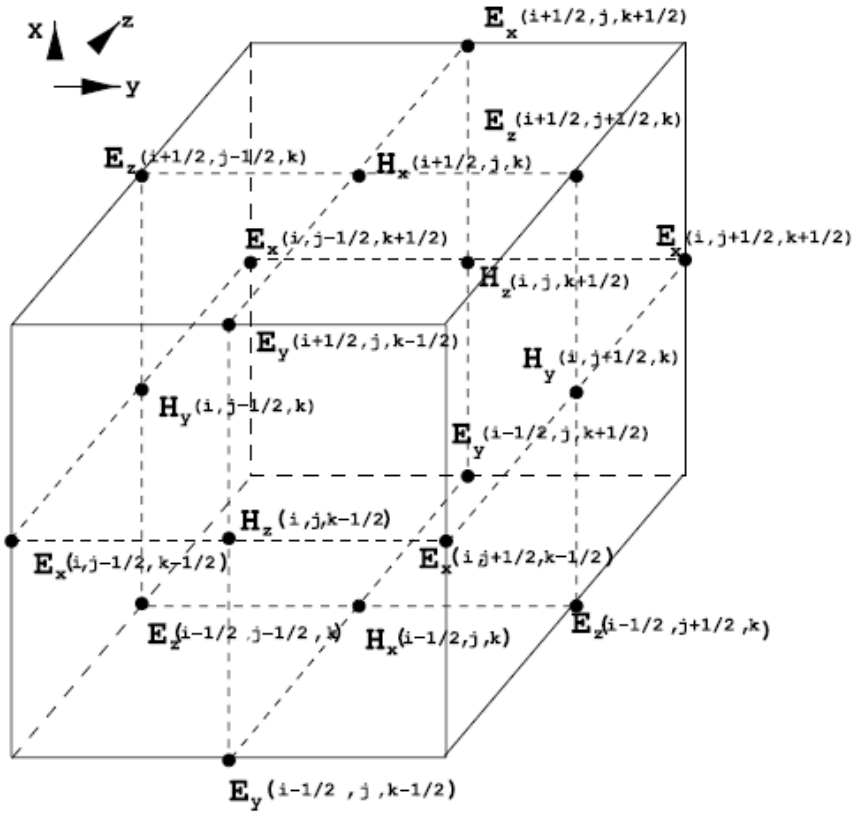

Figure 3.1: The Yee cell used for the finite difference time domain method. The H values appear on the cube face centers while the E values appear on the edge centers.

$$\nabla \cdot \vec{B} = \rho_m \tag{3.5}$$

along with

$$\vec{B} = \mu \vec{H} \tag{3.6}$$

$$\vec{D} = \varepsilon \vec{E} \tag{3.7}$$

σ_e and σ_m are the electric and magnetic conductivities with ρ_e and ρ_m as the electric and magnetic charge densities. These equations can be separated into coordinate system components. For instance, looking at the x component of (3.3), we find

$$\varepsilon \frac{\partial \vec{E}_x}{\partial t} = \frac{\partial \vec{H}_z}{\partial y} - \frac{\partial \vec{H}_y}{\partial z} - \sigma_e \vec{E}_x \tag{3.8}$$

Manipulating the terms of the Taylor expansions of $f(u+\Delta u)$ and $f(u-\Delta u)$, we can find the central difference approximation for the derivative of f(u)

$$\frac{\partial f}{\partial u} = \frac{f(u + \Delta u/2) - f(u - \Delta u/2)}{\Delta u} + O(\Delta u^2) \qquad (3.9)$$

where $O(\Delta u^2)$ represents higher order terms which are dropped from the equation because they are proportional to higher order powers of Δu which is assumed to be very small. Still, dropping these terms causes some error in the approximate answer.

We now apply this approximation to the six equations formed by the components of (3.2) and (3.3) to obtain six equations for each component of E and H [7]. In these equations, the E fields are measured at the integer time steps while H fields exist at the half time steps. From these equations it also obvious that the E field at any point and time depends only on the value of the E field at that point one time step earlier and the value of the H field at the four closest points one-half time step earlier. After a source is included, only boundary conditions need to be defined on the grid, and the problem can be solved by an iterative solution of the finite difference equations.

3.3 Simulation Program and Other Tools

The main simulation program is written in C++ and was compiled and run on the HPUX machines in the Department of Electrical and Computer Engineering at Ohio State. There are two steps to obtaining the complete solution for a new resonator geometry. First, the frequency response of the resonator must be calculated to find Mode 1. Next, the FDTD code is run again, this time calculating the field distribution at that frequency.

In the first step, the program excites an FDTD gridded geometry and computes the fields iteratively in time for a specified number of time steps. The excitation in this case is not important as long as it covers the frequency range of interest [7]. The field values at a few points inside the head or phantom are recorded throughout the process. At the end of the process, the time history of the fields is converted to the frequency domain by fast Fourier transform (FFT) in MATLAB. Mode 1 can then be identified on the frequency response plot. The geometry can then be tuned to achieve the appropriate Mode 1 if the peak is shifted.

Once Mode 1 is identified for the geometry, the code is run a second time with the frequency of Mode 1 specified. When running with a frequency specified, the program does not record the time values but runs a runs a discrete Fourier transform (DFT) at the Mode 1 frequency at the end to determine the field distribution. The field data can then be loaded into MATLAB and plotted as an image.

Also used on this project are the GridView program and two MATLAB scripts, one for the analysis each step in the simulation processes. The GridView program is a graphical interface with which to create resonator geometries on an FDTD grid. The geometry is viewed as a planar-sliced 2D image gridded at the specified thickness. Each grid square can then be changed to various materials which are recognized by the FDTD program and assigned appropriate electrical properties. Figure 3.2 shows a typical plane slice of the resonator and head with different colors representing different materials.

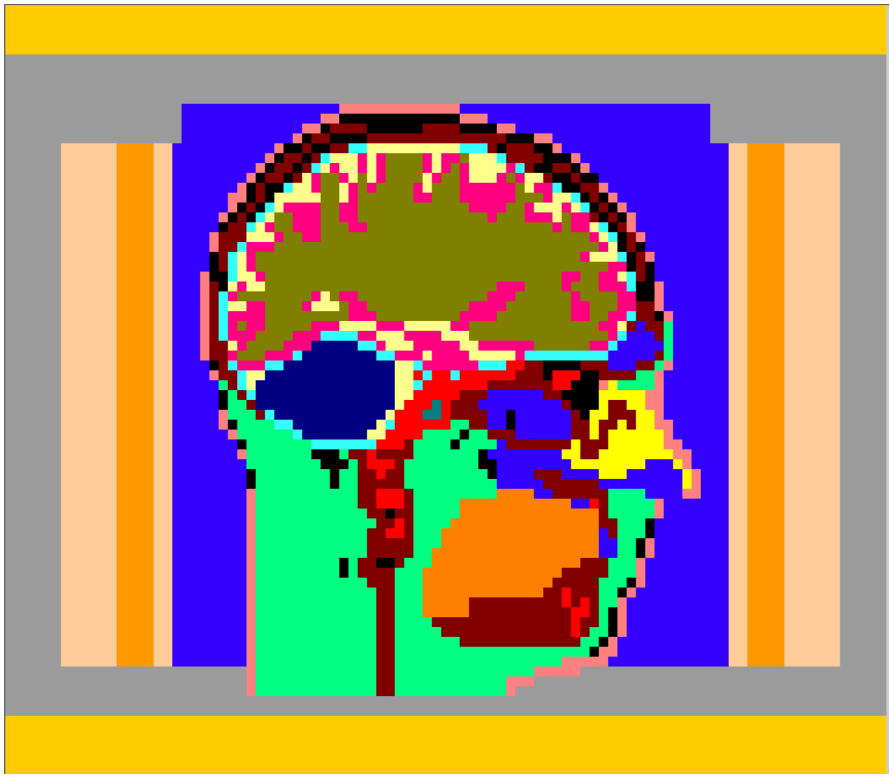

Figure 3.2: A sagittal slice of the 18 tissue head model in a $(4mm)^3$ grid. The head is surrounded by air (blue) and the resonator.

3.4 The Human Head Model and Baseline TEM Resonator

The head model shown in Figure 3.2 is a $(4\ mm)^3$ model, meaning that each FDTD cell is 4 mm x 4 mm x 4 mm. Within each cell a single material is defined. In this head model, there are 18 distinct materials in the head. A listing of the tissues and their properties can be found in Table 3.1 [7]. The model was created by a physician who assigned a material to each cell of a 1.5 T image of a human head that was gridded with FDTD cells.

The baseline TEM resonator used was 21.2 cm long in length. It is fed with a 4-port excitation, and resonates at 342 MHz when loaded with the head model. The frequency response of the baseline resonator is shown in Figure 3.3 and the normalized distribution of Mode 1 is shown in Figure 3.4.

Tissue	Density (kg/m^3)	Relative Permittivity	Conductivity (S/m)
Blood	1060	57.50	1.700
Bone – Cancellous	1850	21.84	0.209
Bone – Cortical	1850	13.91	0.100
Cartilage	1100	44.82	0.620
Cerebellum	1040	54.40	0.880
Cornea	1050	55.40	1.050
Cerebro Spinal Fluid	1060	69.08	2.300
Dura	1020	52.23	0.770
Fat	920	5.14	0.040
Gray Matter	1040	57.05	0.839
Mixed Grey & White Matter	1040	49.45	0.669
Mucosa	1020	52.69	0.690
Muscle	1040	65.57	0.938
Nerve	1040	36.80	0.400
Skin	1100	43.07	0.540
Tongue	1040	59.64	0.800
Vitreous Humor	1010	68.30	1.550
White Matter	1040	41.85	0.499

Table 3.1: Tissues found in the 18 tissue human head model and their properties at 340 MHz.

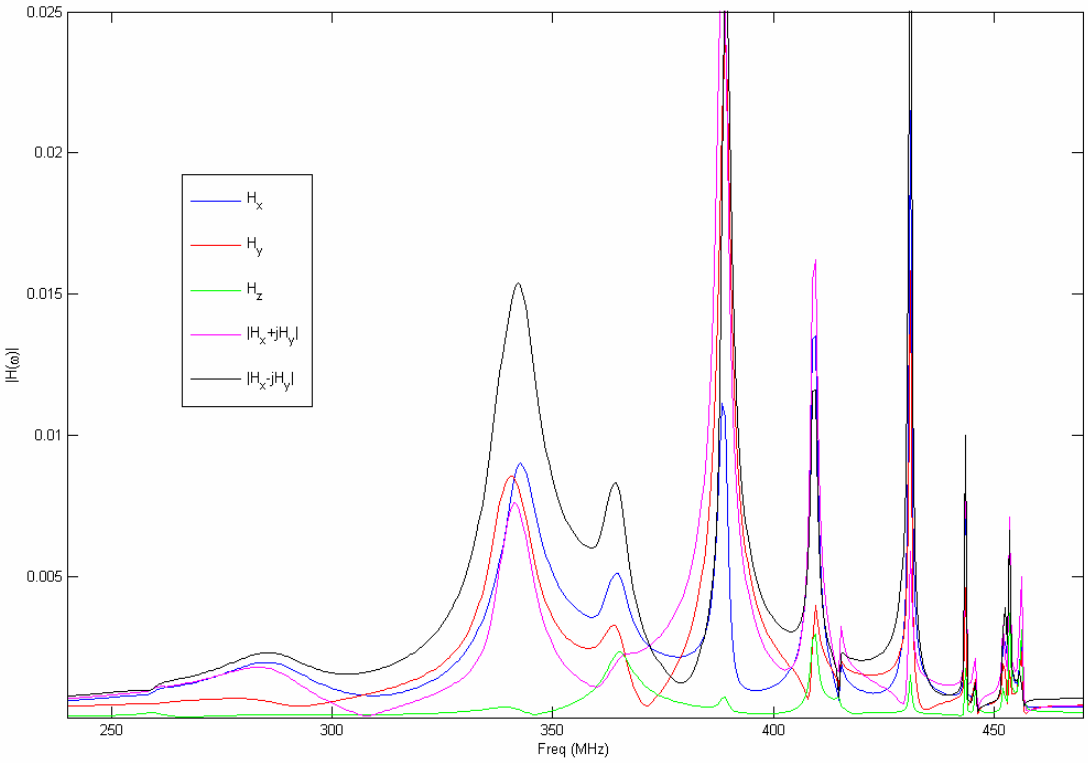

Figure 3.3: Frequency response of the 21.2 cm resonator. Here the resonator has no dielectric filling but is loaded with the human head. Mode 0 appears with a very low Q around 280 MHz and Mode 1 appears at 342 MHz.

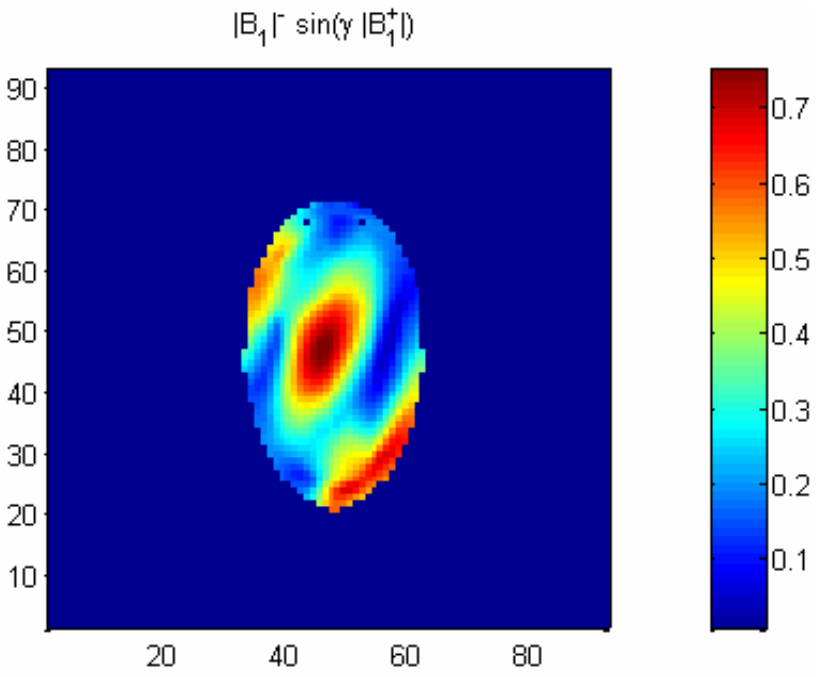

(a)

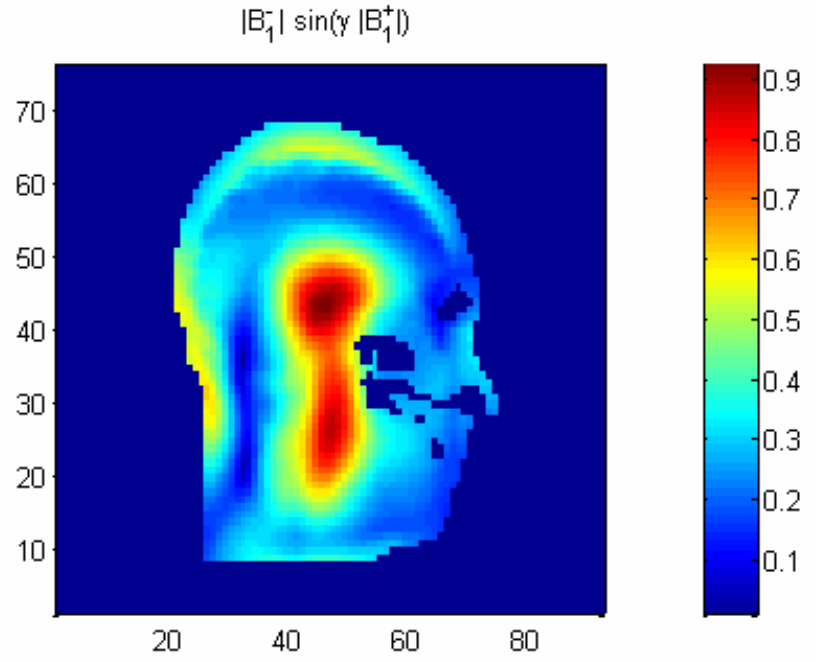

(b)

Figure 3.4: Axial (a) and sagittal (b) slices showing the normalized field distribution of the baseline resonator at Mode 1 (342 MHz)

CHAPTER 4

RESONATOR COIL DESIGN

The process of finding an optimal design for the resonator coil is a challenging one due to the large space of possibilities to search and the relative slowness of the simulation process. It is possible to produce many simulations but still be unable say whether any design is optimal or not. Therefore, this chapter will address the important trends found in simulating the resonator coil and provide some suggestions for directing future simulations.

4.1 The TEM Resonator Filled with Dielectric

As discussed earlier, the goal of these simulations is to spread out the central peak found in Figure 3.4 so that imaging may be conducted over a larger area of the head. To accomplish this, the resonator cavity was first filled with a lossless dielectric material. In a real design, this material could be titanium dioxide which has no MRI signal and can be compressed to give high dielectric constants. Since the head model is also located in the resonator cavity, the entire cavity could not be filled with dielectric. To keep the design realistic, a small clearance was used between the head and dielectric material. This left dielectric material around the struts and outer portions of the resonator. In Figure 4.1 the basic resonator filled with dielectric is

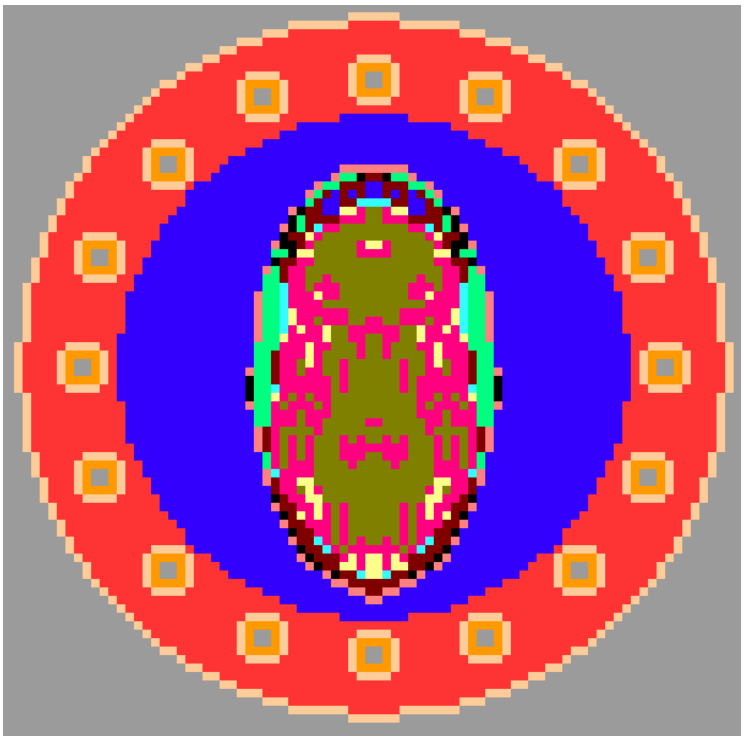

Figure 4.1: An axial slice of the resonator fully filled with dielectric (red). The air gaps appear around the outer edges and around the struts because of the way PEC boundary conditions are assigned in the code.

shown. The red material is the inserted dielectric while blue, peach, and grey are air. The orange material is the strut dielectric sleeve which is surrounded by the conducting outer strut (not shown). Despite not being completely filled with dielectric, this paper will refer to this design as "fully loaded" for simplicity.

In the baseline case shown in Figure 3.4, the permittivity of the dielectric filling is set to 1 to simulate air. As expected, simulations showed that increasing the permittivity of the filling lowered the resonant frequency of Mode 1. The permittivity dependence of the Mode 1 resonant frequency is shown in Figure 4.2. The plot shows that the frequency drops quickly away from the desired value of 343 MHz even for small permittivity values.

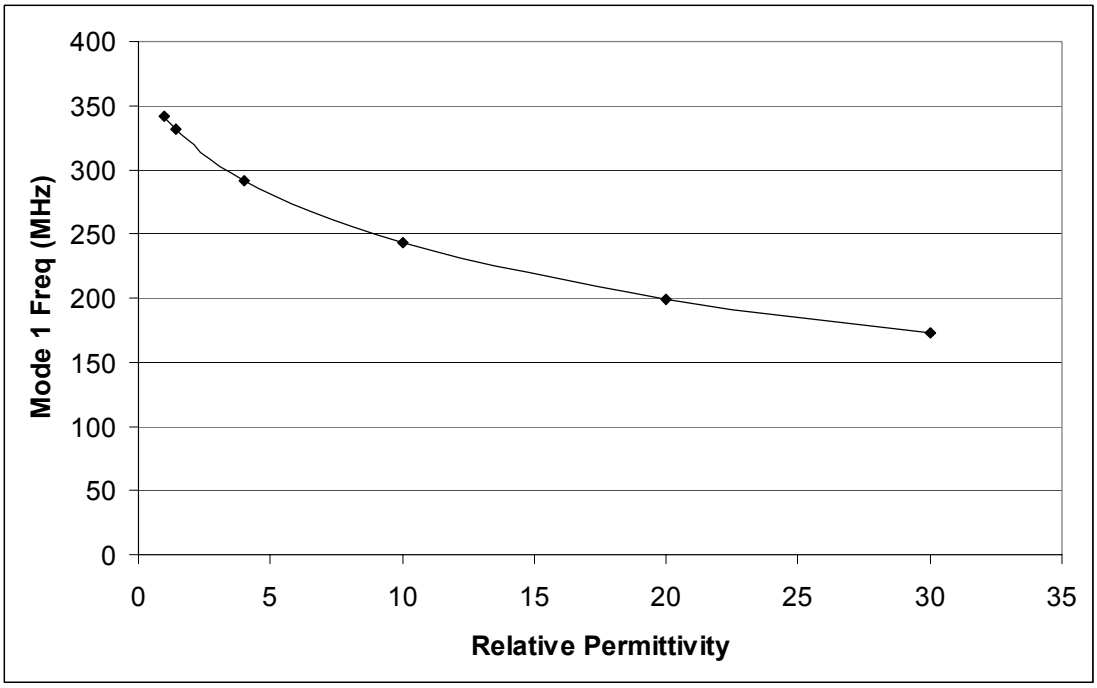

Figure 4.2: The Mode 1 resonant frequency vs. relative permittivity of the dielectric filling for the fully loaded case.

After the resonant frequencies of each design were computed, a second simulation was performed to find the field distribution at that frequency. Some of these field distributions are shown in Figures 4.3 (axial) and 4.4 (sagittal). Clearly the progressive increase in permittivity is spreading the peak in the axial plane. However, since the resonant frequency is also decreasing, it is unclear from these results whether the improved homogeneity is caused only by the dielectric or if the lower resonant frequency plays some part. To be useful for imaging at 8 T, the resonant frequency must be 343 MHz.

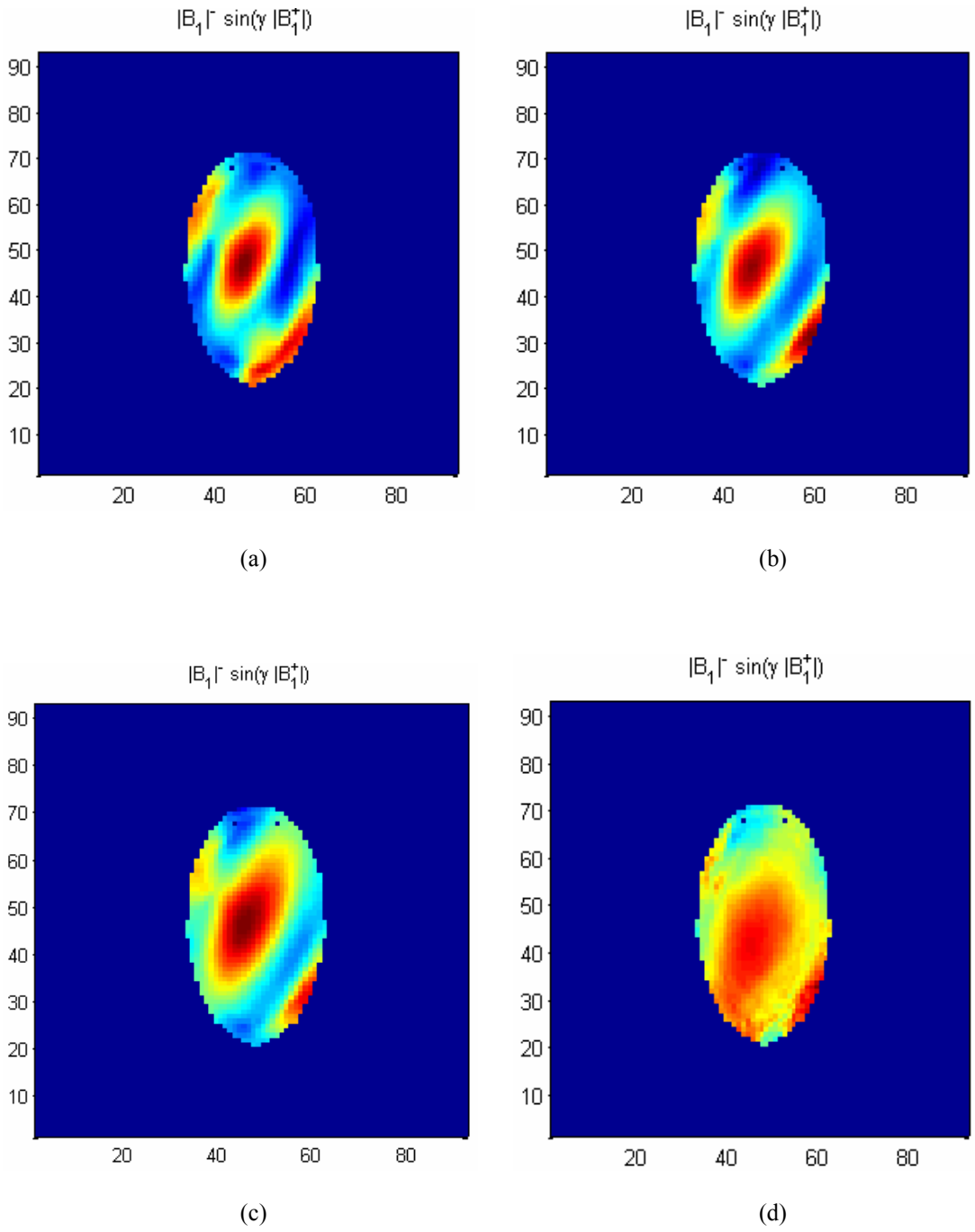

Figure 4.3: Axial slices of the normalized field distribution in the head for the fully loaded case. This shows the baseline $\varepsilon_r = 1$ case (a), as well as $\varepsilon_r = 4$ (b), $\varepsilon_r = 10$ (c), and $\varepsilon_r = 30$ (d) cases.

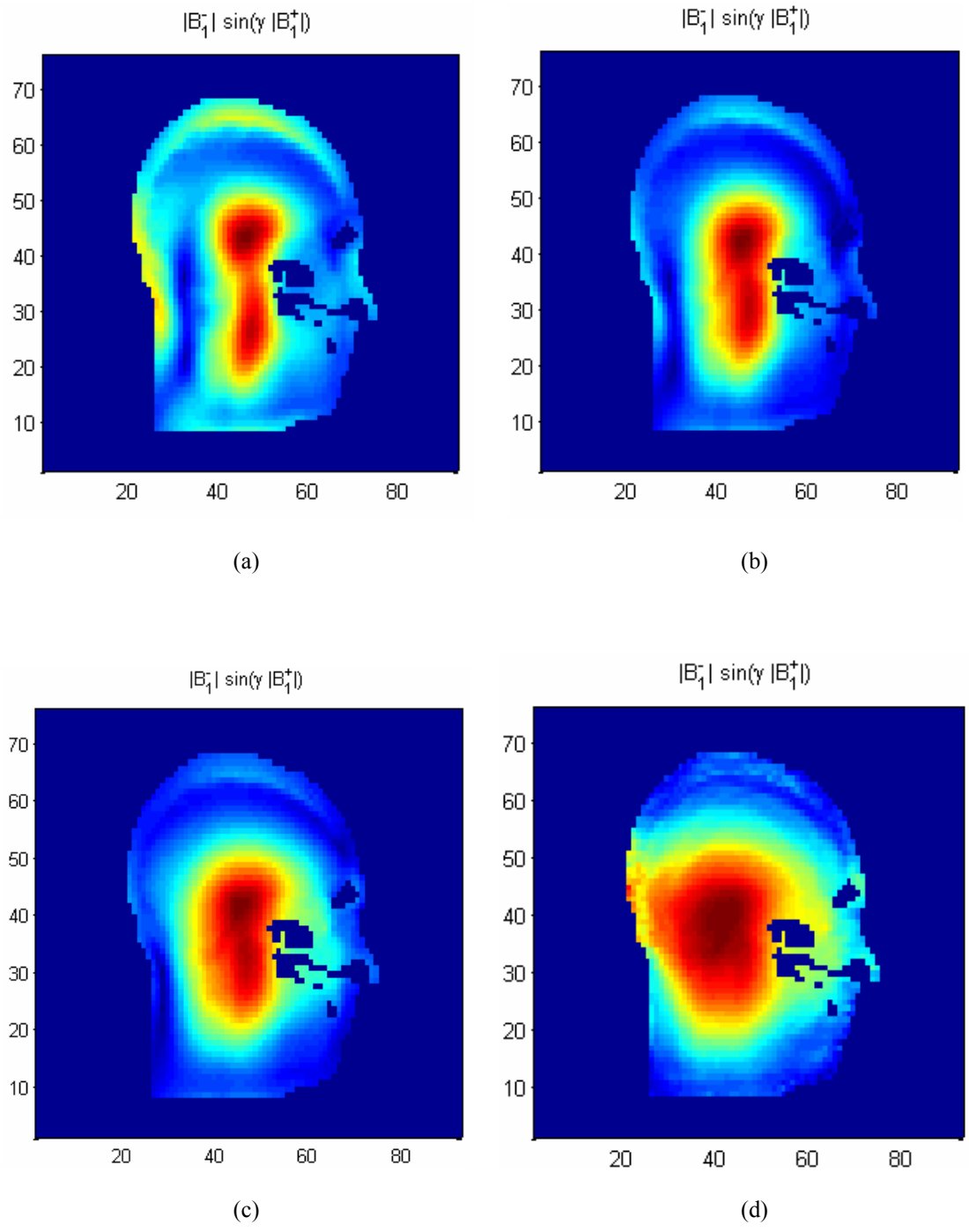

Figure 4.4: Sagittal slices of the normalized field distribution in the head for the fully loaded case. This shows the baseline $\varepsilon_r = 1$ case (a), as well as $\varepsilon_r = 4$ (b), $\varepsilon_r = 10$ (c), and $\varepsilon_r = 30$ (d) cases.

Figure 4.5: Sagittal slice of the 4 cm resonator. The blue material is air like the gray so its unorthodox shape does not affect the results.

4.2 The Shortened TEM Resonator

In order to shift the frequency back towards the desired frequency of 343 MHz, the length of the resonator must be shortened, forcing the resonant frequency of the transmission lines upwards. The first shortened resonator that was attempted was 4.4 cm in length for use with high dielectric constants. This was estimated to be the shortest resonator possible with a $(4mm)^3$ grid because of the coarseness of the grid. The actual length expected to be needed to shift the frequency high enough was actually even shorter at around 3 cm. The geometry of the 4.4 cm resonator is shown in Figure 4.5.

When solved, the 4 cm resonator what appeared to be Mode 1 was actually Mode 2 because Mode 0 does not exist for this resonator. Contrary to expectations, Mode 1 was found at a much higher frequency than desired, at around 522 MHz and 492 MHz for permittivity of 60 and 76, respectively. One could conclude that

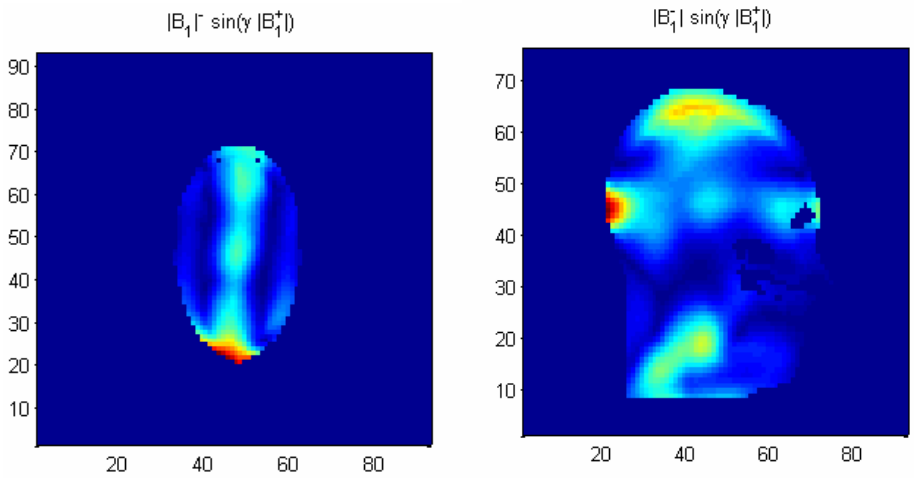

Figure 4.6: Axial (a) and sagittal (b) field distributions for the 4 cm resonator with permittivity 60.

shortening the resonator had a greater effect on the resonant frequency than expected, but a more reasonable answer is that the dielectric filling caused less of a shift than expected. The approximations for the shift caused by the filling assumed a completely filled resonator which was not true for the actual design. Thus, we find that the 4 cm resonator placed the resonance frequency higher than desired.

In Figure 4.6 the field distributions of the 4 cm resonator with permittivity of 60 are shown. The results for a permittivity of 76 are very similar. From the distributions, it is clear that the short length of the resonator inhibits a smooth distribution of the magnetic field in any location. In the sagittal slice (4.6b), this looks much like Mode 0, but from the axial slice (4.6a), we can see that the central peak characteristic of Mode 1 still exists.

Since the results for the 4 cm resonator were unsatisfactory, the resonator was lengthened to 10 cm (Figure 4.7). This longer resonator would mean less of frequency shift from the full length case and possibly a better field distribution.

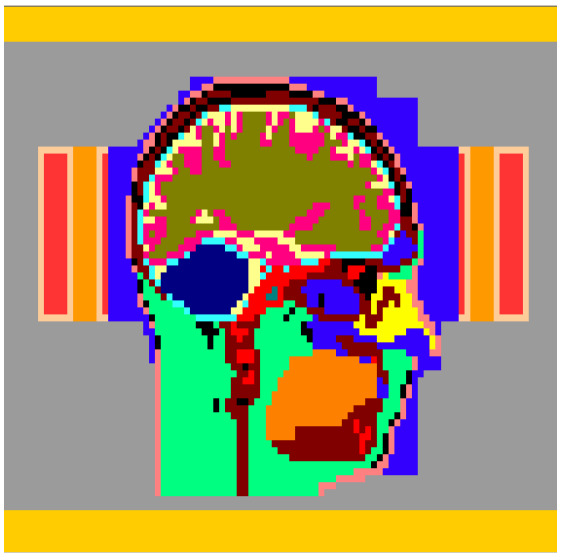

Figure 4.7: Sagittal slice showing the 10 cm resonator filled with dielectric. The blue material is air like the gray so its unorthodox shape does not affect the results.

Looking at Figure 4.8, we see that the 10 cm resonator shows much better results than the 4 cm. Moreover, the Mode 1 frequency has dropped to 278 MHz and 262 MHz for permittivity 50 and 60, respectively. Thus the 343 MHz resonance with this range of dielectric constants is expected to be achieved with a resonator of approximately 8 cm after tuning. The field plots also retain the shape of the full length resonator, whereas for the 4 cm case, they looked only very remotely like the full length resonator. The field peaks in the 10 cm case have spread significantly compared to the baseline case. In fact, the 10 cm resonator shows more homogeneity than the full length case with permittivity 10 (Figure 4.3c and Figure 4.4c) even though the frequency is higher with the 10 cm resonator. This answers the question of whether the lower frequency is the factor that is spreading the peak. Clearly, it is not the only factor since the 10 cm resonator at 278 MHz outperforms the full length device at just 243 MHz. The higher permittivity in the shorter resonator is playing the main role.

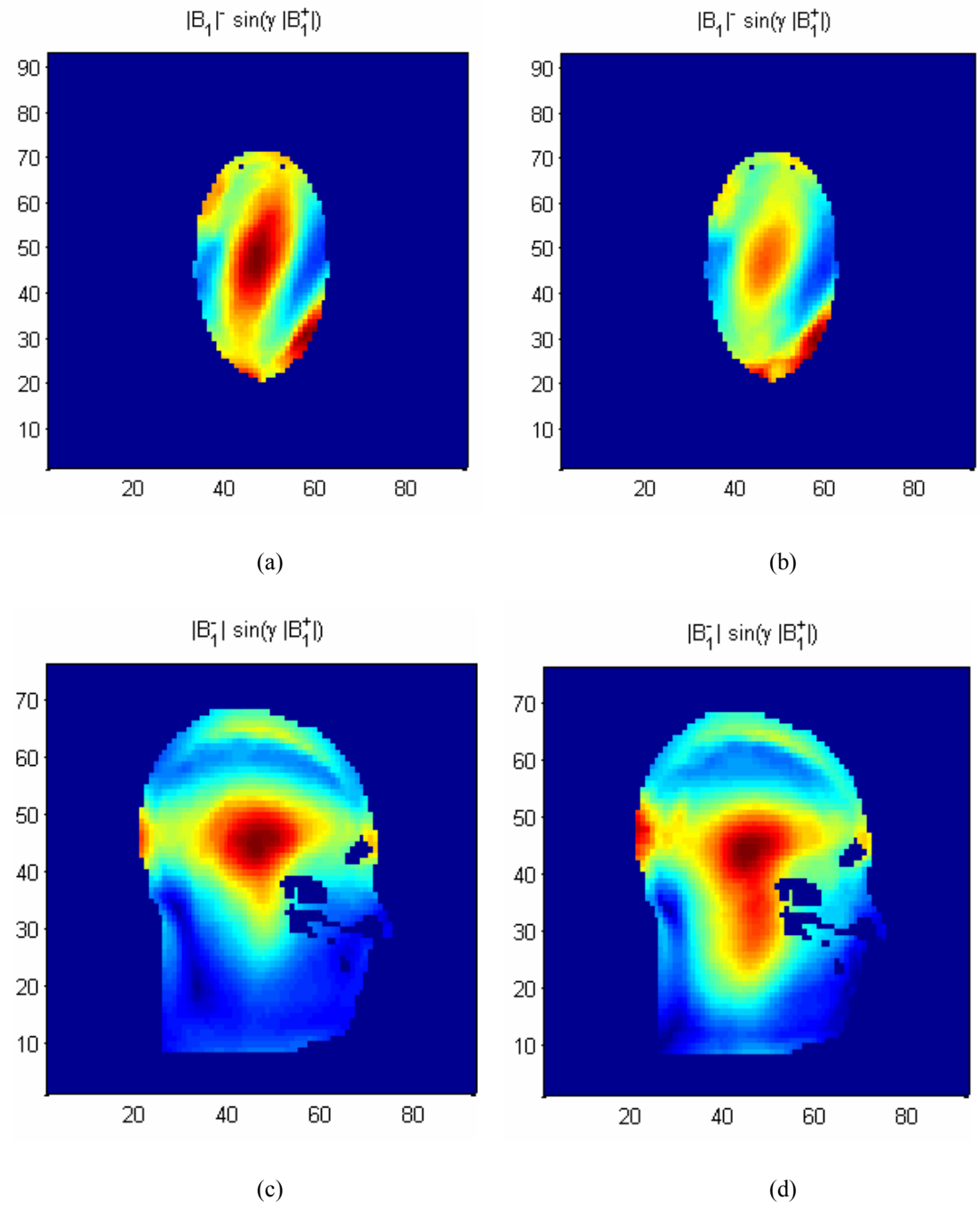

Figure 4.8: Axial and sagittal slices of the normalized field distribution for the fully loaded 10 cm resonator with permittivity 50 (a,c), and 60 (b,d).

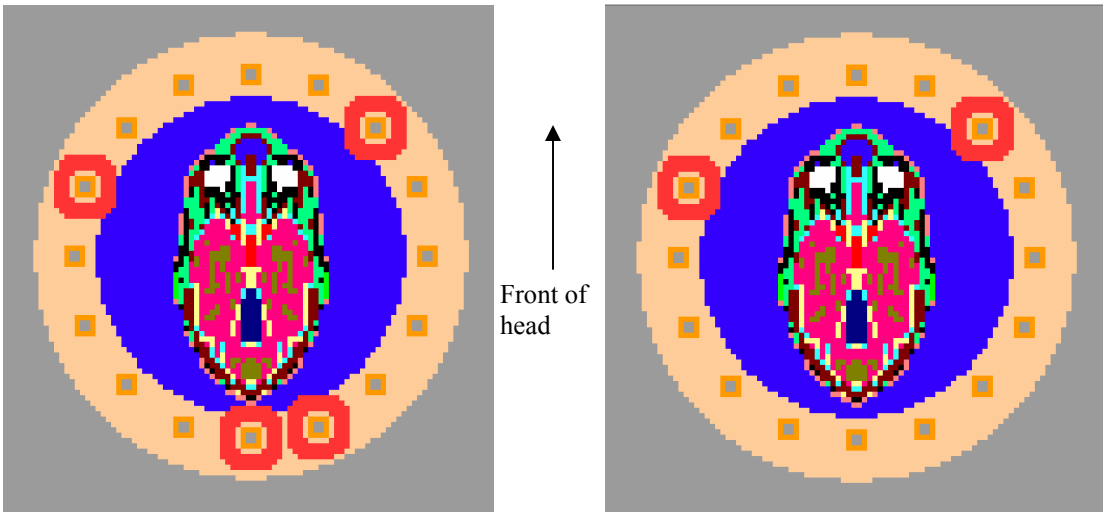

(a) (b)

Figure 4.9: Axial slices of the partially loaded resonator with 4 struts loaded (a) and 2 struts loaded (b)

4.3 The Partially Filled Resonator

As an additional study, a few simulations were run with small portions of the resonator loaded by the dielectric filling. To simulate real world use, the filling was placed in the grid as rings that could be placed around the struts. The rings were made to be much shorter than length of the resonator and two loading heights were attempted. Three different designs were used. The first used the strut loading pattern (Figure 4.9a) and aligned vertically between the nose and eyes (grid values 31 – 42 in the sagittal plots). The second used the same strut loading pattern (Figure 4.9a), but was placed higher in the vertical dimension. It was aligned with the widest part of the head (grid values 40 – 55 in the sagittal plots). A third model was loaded with a different strut pattern (Figure 4.9b), but used the same vertical alignment as the second model.

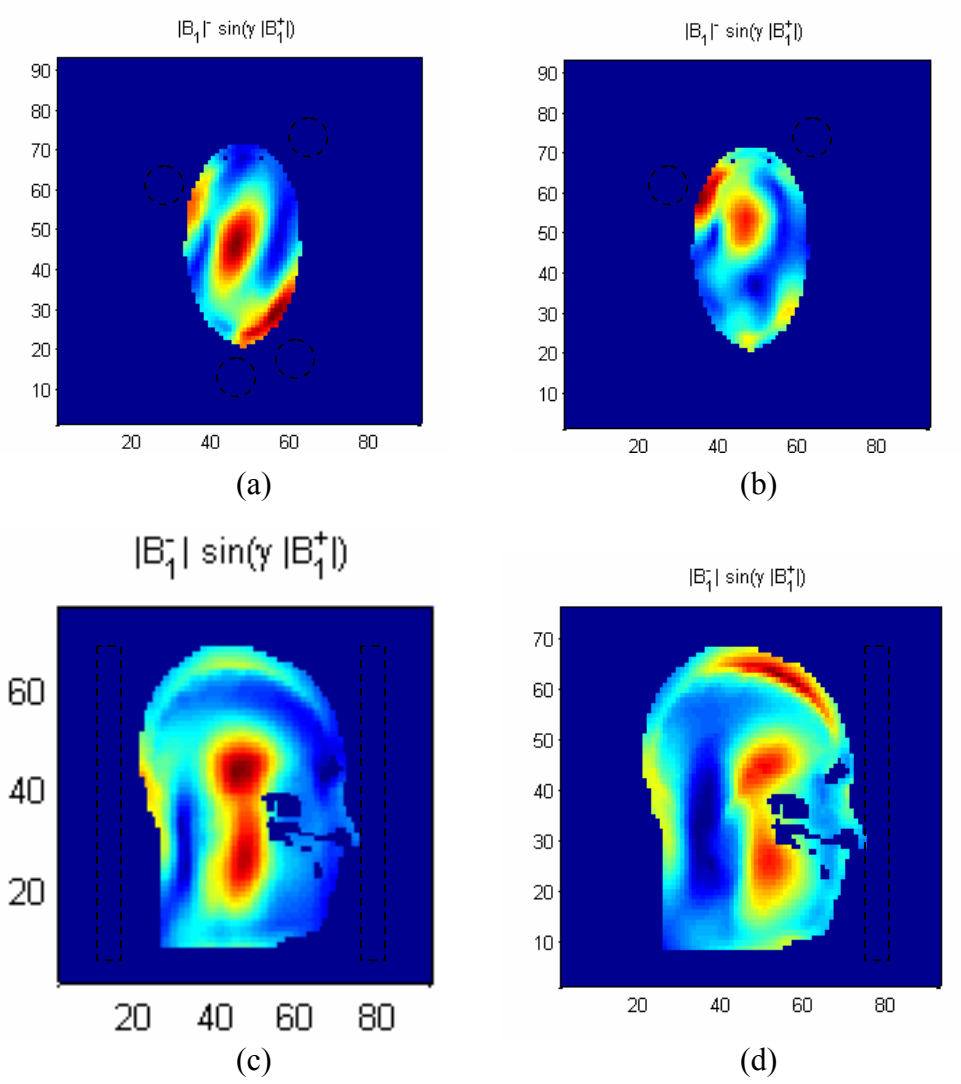

Figure 4.10: Axial (a,b) and sagittal (c,d) normalized field distributions for the partially loaded resonators shown in Figure 4.9a (a,c) and Figure 4.9b (b,d). Loaded struts are represented by dotted lines.

The first model (4 struts loaded at low height) yielded a result that showed very little change from the baseline image (Figure 4.10a,c). The second model (4 struts loaded at higher location) produced strange results that suggest the resonant frequency selected was incorrect. Further work is being done on this model to confirm the field pattern. Finally, the third model (2 struts loaded at high location) showed the result that was expected (Figure 4.10b,d) suggesting that the asymmetric

loading is much more effective in moving the field center. This is probably due to effects being canceled by struts on opposite sides of the resonator. It should also be noted that the frequency shift from these loading patterns was very small even though the permittivity used was 50. The resonant frequencies in each case were between 325 MHz and 340 MHz.

CHAPTER 5

CONCLUSIONS

5.1 Summary of Results

In these simulations, the behavior of the resonator has confirmed several theoretical principles about the way the resonator functions. First, loading the resonator with a dielectric filling near the struts was expected to lower the resonant frequency, and it was found to lower the frequency significantly (Figure 4.2). Second, shortening the length of the coil was expected to offset this decrease and raise the resonance frequency. This is clearly true as Mode 1 resonant frequencies are found at around 500 MHz for the 4 cm coil while they are found at less than 200 MHz for similar dielectric constants in the 21.2 cm coil. Finally, we expected that loading the resonator with a dielectric material more similar to that of the head would yield a more homogeneous magnetic field in the head. This is confirmed by Figure 4.3 and 4.4 which show how the field pattern spreads as the dielectric constant of the filling is increased.

If an "optimal" design were to be chosen, it would be the 10 cm resonator loaded with a dielectric of permittivity 60. This provided quite a homogenous distribution in the center of the skull (Figure 4.8b,d) and kept the frequency (262 MHz) reasonably near 343 MHz. However, work should be continued in this area because it appears that a more optimal design can be found with a resonator of length

around 8 cm and possibly a higher dielectric constant. This would probably provide an even greater homogeneity than the current designs.

5.2 Future Work

Now that a study of the response of the resonator to basic geometry and loading changes has been completed, the way is clear for future exploration and a design/build experiment. It has been shown that a result with good homogeneity and reasonable resonant frequency has been obtained with a 10 cm resonator and dielectric material with relative permittivity of 60. Simulations should be run on an 8 cm resonator to find a permittivity which will enable the maximum homogeneity while resonating at a frequency near 343 MHz. Such a resonator could easily be tuned to the Larmour frequency at which point it could be built and tested using Ohio State's 8 T MRI device.

Some other geometry changes can be explored such as creating a small air pocket out of the dielectric around each strut to increase the resonant frequency without changing the length of the resonator and without significantly affecting the homogeneous field pattern. Further, the effects of loading single struts to shift the field pattern to the desired location is promising if the right patterns can be found. This could be quite beneficial because the small amount of dielectric material used can shift the field patterns greatly, but only causes a small change in the resonant frequency. Finally, placing the dielectric material higher or lower may also generate useful results showing that the peak could be shifted vertically in the head.

These projects can all be completed in much less time now that the original project has worked out many of the difficulties discovered on the way. Problems in transferring the code from Linux to Unix and improper changing of the geometry delayed the completion of the project and rendered some earlier results invalid. However, now that these issues are known, simulations can be carried out much more quickly and with more confidence so that the aforementioned suggestions could be completed soon. Ultimately though, a hybrid code combining FDTD with FEM could speed up the 2-3 day simulation cycle considerably.

BIBLIOGRAPHY

[1] P. C. Lauterbur, "Image formation by induced local interactions: example employing nuclear magnetic resonance," *Nature*, vol. 241, pp. 190–191, 1973.

[2] Z. H. Cho, J. P. Jones, M. Singh, *Foundations of Medical Imaging*. New York: John Wiley and Sons, 1993

[3] Y. Lvovsky, P. Jarvis, "Superconducting Systems for MRI—Present Solutions and New Trends," *IEEE Trans. on Appl. Superconductivity*, vol. 15, iss. 2, pp. 1317-1325, 2005.

[4] P. Marzola, F. Osculati, A. Sbarbati, "High field MRI in preclinical research," *European Journal of Radiology,* vol. 48, iss. 2, pp. 165-170, 2003.

[5] E. Yacoub, A. Shmuel, J. Pfeuffer, P.-F. Van De Moortele, G. Adriany, P. Andersen, J. T. Vaughan, H. Merkle, K. Ugubil, X. Hu, "Imaging brain function in humans at 7 Tesla," *Magn. Reson. Med.*, vol. 45, iss. 4, pp. 588-594, 2001.

[6] T. S. Ibrahim, R. Lee, A. M. Abduljalil, B. A. Baertlein, P.-M. L. Robitaille, "Dielectric resonances and B1 field inhomogeneity in UHFMRI: computational analysis and experimental findings", *Magn. Reson. Imag.*, vol. 19, iss. 2, pp. 219-226, 2001.

[7] T. S. Ibrahim, "Design of radiofrequency coils for magnetic resonance imaging applications: a computational electromagnetic approach", Doctoral Dissertation, The Ohio State University, Columbus, Ohio, 2002. The Ohio State University Science and Engineering Library.

[8] F. Bloch, "Nuclear induction," *Phys. Rev.*, vol. 70, pp. 460–474, 1946.

[9] E. M. Haacke, R. W. Brown, M. R. Thompson, R. Venkatesan, *Magnetic Resonance Imaging: Physical Principles and Sequence Design*. New York: John Wiley and Sons, 1999.

[10] J. T. Vaughan, H. P. Hetherington, J. O. Otu, J. W. Pan, and G. M. Pohost, "High frequency volume coils for clinical NMR imaging and spectroscopy," *Magn. Reson. Med.*, vol. 32, pp. 206-218, 1994.

[11] E. C. Hayes, W. A. Edelstein, D. F. Schenck, O. M. Mueller, and M. Eash, "An efficient highly homogenous radiofrequency coil for whole-body NMR imaging at 1.5 T," *J. Magn. Reson.*, vol. 63, pp. 622-628, 1985.

[12] B. A. Baertlein, O. Ozbay, T. S. Ibrahim, R. Lee, A. Kangarlu, and P.-M. L. Robitaille, "Theoretical model for an MRI radio frequency resonator," *IEEE Trans. Biomed. Eng.*, vol. 47, pp. 535-546, 2000.

[13] E. J. Butterworth, E. G. Walsh, J. W. Hugg, "A TiO_2 dielectric filled toroidal radio frequency cavity resonator for high-field NMR," *NMR in Biomed.*, vol.14, iss. 3, 2001.

[14] K. S. Yee, "Numerical solution of initial boundary value problems involving Maxwell's equation in isotropic media," *IEEE Trans. Antennas Propagation,* vol. AP-14, iss. 4, pp. 302-307, 1966.